

Hybrid Beamforming via Programmable Unitary RF Networks

Nikola Zlatanov and Damir Salakhov

Abstract

Conventional hybrid beamforming architectures are often compared with one another and with the fully-digital architecture under the same *radiated* antenna power. However, the physically relevant budget is the power injected by the RF-chain outputs into the passive analog RF network, which is then usually transferred to the antenna ports in a contractive (lossy) manner. This issue is especially pronounced for fully-connected splitter–phase-shifter–combiner networks, whose physical power transfer remains contractive even under ideal passive-component assumptions. Motivated by this injected-power viewpoint, this paper proposes a hybrid beamforming architecture based on a programmable unitary RF network. Under ideal passive-component assumptions, all injected RF-chain power reaches the antenna ports without loss.

The analog RF network is realized as an *interlaced mixer–phase* architecture consisting of fixed (non-programmable) mixing layers interleaved with programmable diagonal phase-shifting layers. We derive a closed-form digital beamformer and a low-complexity programming method for the analog beamformer, yielding a hybrid precoder that closely matches the fully-digital precoder. When the programmed analog subspace contains the target subspace, the resulting hybrid precoder exactly reproduces the fully-digital precoder under the same injected-power constraint. The depth analysis provides a stream-aware necessary guideline for when such containment becomes plausible, and the numerical results show that near-exact recovery is reached once the depth is sufficiently large. Narrowband simulations with continuous and quantized phases, benchmarked against the fully-digital architecture, the physically modeled fully-connected phase-shifter baselines, and an ideal-lossless Butler/DFT beam-selection baseline under equal total injected RF-chain power, show that the continuous-phase and 6-bit realizations of the proposed architecture are nearly indistinguishable from the fully-digital benchmark and achieve significant gains over the baseline hybrid beamforming architectures.

Index Terms

N. Zlatanov and D. Salakhov are with Innopolis University, Innopolis, 420500, Russia (e-mails: n.zlatanov@innopolis.ru and d.salakhov@innopolis.ru).

Hybrid beamforming, unitary RF networks, interlaced mixer–phase architectures, phase quantization, Grassmann manifold.

I. INTRODUCTION

Massive multiple-input multiple-output (MIMO) systems rely on linear precoding to suppress multiuser interference and to exploit array gain. Fully-digital precoding is the natural baseline; however, it requires one radio-frequency (RF) chain per antenna, which is often infeasible in large arrays due to power, cost, and routing constraints [1]. Hybrid analog–digital beamforming architectures address this bottleneck by combining a high-dimensional analog network with a low-dimensional digital stage. Typically, these architectures comprise r RF-chains and N antennas, with $r \ll N$, and are able to support $S \leq r$ data streams.

Most hybrid-beamforming papers describe the analog stage through an abstract matrix \mathbf{F}_{RF} and then compare architectures after normalizing the composite precoder $\mathbf{F}_{\text{RF}}\mathbf{F}_{\text{BB}}$ to the same radiated power, where \mathbf{F}_{BB} is the digital precoder. This is appropriate when the goal is to compare hybrid-beamforming architectures at equal radiated power from their antennas. However, such a comparison does not reveal how much of the physically relevant power, which is the power injected by the RF-chains, actually reaches the antenna ports. Once the analog stage is interpreted as a physical analog RF network between the RF-chain outputs and the antenna ports, it becomes clear that not all power injected by the RF-chains into the analog RF network reaches the antenna ports, even under ideal passive-component assumptions. As a result, a more physically relevant comparison between beamforming architectures is under a fixed total injected-power budget by the RF-chains.

This issue has already been highlighted in realistic RF analyses of hybrid precoders [1], [2], which showed that fully-connected splitter–phase-shifter–combiner networks can be strongly contractive even under ideal passive-component assumptions. As a result, analog RF networks that conduct unitary (lossless) power transfer have been proposed, such as the Butler/DFT beamforming networks [2] and the lens- and beamspace-based front-ends [1], at the cost of substantially lower abilities for analog transforms.

Among the common fully-connected phase-shifter hybrid beamforming architectures, used also as baselines in this paper, this issue is particularly visible in [3], [4]. When these architectures are interpreted through their physical splitter–phase-shifter–combiner implementations, the resulting transfer from the RF-chain outputs to the antenna ports is contractive rather than semi-unitary.

Consequently, under equal injected power, only a fraction of the RF-chain power reaches the antennas, while the remaining power is absorbed in the combining/termination circuitry or is otherwise unavailable for radiation. This is precisely the effect that equal-radiated-power normalization obscures.

From the viewpoint of RF transport efficiency, the maximal transfer of power occurs when the underlying $N \times N$ analog RF network is unitary. In that case, the induced $N \times r$ transfer of power from the r driven RF-chain inputs to the N antenna ports is semi-unitary and thereby the analog beamformer transfers the injected power exactly. However, an analog beamformer that conducts semi-unitary transfer of power is only one of the two important aspects. The second important aspect is that the analog beamformer must have full-expressiveness, which means that it can be programmed to express any r -rank semi-unitary matrix.

This paper proposes and studies a hybrid beamforming architecture whose analog beamformer conducts power-preserving RF transport from the RF-chains to the antenna ports and is programmed via its phase-shifter settings to realize the desired analog subspace. We derive a closed-form digital beamformer and a low-complexity programming method for the analog beamformer, which result in a hybrid beamforming precoder that closely matches the fully-digital precoder. The numerical results then show that near-exact recovery is reached once the depth is sufficiently large in the considered setting.

Programmable universal unitary analog processors offer a natural way to realize such power-preserving analog stages. Universal unitary analog processors based on interferometric meshes are well known in photonics [5], [6]. More recently, *interlaced mixer-phase* architectures—fixed mixing layers interleaved with programmable diagonal phase layers—have emerged as a robust route to programmable unitary transforms in both photonic and microwave settings [7], [8]. This paper leverages such universal unitary analog processors to propose and study a new hybrid beamforming architecture.

Recent theory on layered programmable unitary decompositions has established universality criteria for square factorizations of the form $\mathbf{U} = \mathbf{D}_1 \mathbf{V}_1 \mathbf{D}_2 \mathbf{V}_2 \cdots \mathbf{V}_{M-1} \mathbf{D}_M$, and has identified dense mixers such as DFT/complex-Hadamard transforms as especially well-conditioned choices for universal control [8]. Our architecture can be viewed as a repeated-mixer specialization of this broader class; however, the present work addresses a different regime, namely hybrid subspace synthesis with $S \leq r \ll N$, for which full $N \times N$ universality is not required and substantially shallower depths are sufficient.

Specifically, we use the interlaced mixer–phase architecture of [7] as the underlying $N \times N$ analog RF processor. It consists of M programmable diagonal phase-shifting layers interlaced with $M + 1$ fixed mixer layers. For an N -antenna transmitter with r RF-chains, the first r inputs of this analog processor are driven by the RF-chains, the remaining $N - r$ inputs are terminated in matched loads, and the N outputs feed the antenna ports. Because the full analog processor is unitary, the induced analog beamformer from the r driven inputs to the N antenna ports is semi-unitary and therefore preserves the injected power under the ideal matched hardware model.

The hybrid beamforming architecture we propose in this paper is related to two earlier low-loss hybrid beamforming families, but differs from both in analog expressivity. First, sub-connected hybrid precoders connect each RF-chain only to its own antenna subset through a block-diagonal constant-modulus analog matrix [9]. Under standard power normalization, such a structure is non-contractive because its analog columns have disjoint support and unit norm; however, its realizable transmit subspaces are restricted by the fixed partition of the array and do not allow global mixing across subarrays. Second, Butler/DFT-based hybrid architectures realize a fixed orthogonal beamspace transform in the RF domain [2]. In the ideal-lossless case, the RF stage reduces to a selected submatrix of a DFT transform and is therefore also non-contractive, but its analog flexibility is limited to beam selection within a fixed Fourier basis. In contrast, the proposed architecture retains the power-transport advantage of a unitary RF network while making the realizable r -dimensional analog subspace programmable through the diagonal phase layers.

Very recently, MiLAC-based beamforming has been proposed using fully connected tunable-admittance microwave networks, and a hybrid digital–MiLAC factorization was shown, at the matrix-factorization level, to achieve digital-beamforming flexibility with K RF-chains [10]. Our work is close in spirit because it also pursues reconfigurable lossless RF processing beyond conventional phase-shifter networks, but it addresses a different architectural point: instead of a dense tunable-admittance network, we study a structured unitary cascade built from fixed mixers and programmable diagonal phase-shifting layers, which leads naturally to explicit analog programming, depth-scaling insight, and quantized-phase analysis.

Our contributions are as follows:

- 1) We propose a hybrid beamforming architecture in which the analog RF network is built using the interlaced mixer–phase architecture of [7]. The full $N \times N$ processor is unitary, and the induced $N \times r$ analog beamformer from the r RF-chains to the N antenna

ports is semi-unitary. Consequently, under the ideal matched hardware model, the analog beamformer preserves the injected power exactly.

- 2) We derive a closed-form digital beamformer and a low-complexity programming method for the analog beamformer, which result in a hybrid precoder that closely matches the fully-digital precoder. Exact hybrid recovery follows whenever the programmed analog subspace contains the target subspace, and we provide a stream-aware necessary depth guideline for this regime.
- 3) We evaluate the proposed architecture against a fully-digital benchmark, against two physically modeled fully-connected hybrid beamforming baselines, and against an ideal-lossless Butler/DFT beam-selection baseline, all under the same injected power in the narrowband case. The simulations show that the continuous-phase and 6-bit realizations of the proposed architecture are nearly indistinguishable from the fully-digital benchmark and yield significant performance gains over the baseline hybrid-beamforming architectures.

This paper is intended as a proof-of-concept and architectural study of hybrid beamforming with programmable unitary RF networks. Accordingly, aside from the explicit phase-quantization constraint studied in Section III, we ignore hardware non-idealities in the proposed architecture and in all comparator baselines. Therefore, the reported data rates should be interpreted as *idealized upper bounds* under perfect hardware and perfect calibration. Moreover, this paper focuses on the *narrowband* case and leaves the wideband case for future work. In wideband systems, frequency-dependent analog processing would typically require true-time delays or other broadband phase-control mechanisms, which is a natural follow-up direction.

This paper is organized as follows. Section II introduces the narrowband system model, the injected-power viewpoint, the unitary RF-network architecture, the target-matching formulation, and the adjoint phase-programming rule. Section III presents phase-quantized programming. Section IV presents the stream-aware depth guideline. Section V describes the comparator baselines under equal injected power. Section VI provides numerical results, and Section VII concludes the paper.

II. PROBLEM FORMULATION AND HARDWARE MODEL

A. Hybrid beamforming and injected power

We consider a narrowband downlink transmitter with N antennas, r RF-chains, transmitting S data streams, where $S \leq r \ll N$. The hybrid precoder is

$$\mathbf{F} = \mathbf{F}_{\text{RF}} \mathbf{F}_{\text{BB}}, \quad (1)$$

where $\mathbf{F}_{\text{RF}} \in \mathbb{C}^{N \times r}$ is the analog beamformer matrix and $\mathbf{F}_{\text{BB}} \in \mathbb{C}^{r \times S}$ is the digital beamformer matrix. Let $\mathbf{s} \in \mathbb{C}^S$ denote the information vector with $\mathbb{E}[\mathbf{s}\mathbf{s}^H] = \mathbf{I}_S$. The RF-chain output vector is

$$\mathbf{x} = \mathbf{F}_{\text{BB}} \mathbf{s} \in \mathbb{C}^r, \quad (2)$$

and the antenna excitation vector is

$$\mathbf{x}_{\text{ant}} = \mathbf{F}_{\text{RF}} \mathbf{x} = \mathbf{F}_{\text{RF}} \mathbf{F}_{\text{BB}} \mathbf{s}. \quad (3)$$

Throughout the paper, architectural comparisons are performed at equal *injected power*

$$P_{\text{inj}} \triangleq \mathbb{E} \|\mathbf{x}\|_2^2 = \|\mathbf{F}_{\text{BB}}\|_F^2. \quad (4)$$

Assuming ideal matched antennas, the total radiated power equals the antenna-port power,

$$P_{\text{rad}} \triangleq \mathbb{E} \|\mathbf{x}_{\text{ant}}\|_2^2 = \|\mathbf{F}_{\text{RF}} \mathbf{F}_{\text{BB}}\|_F^2. \quad (5)$$

For a general passive RF network one has $P_{\text{rad}} \leq P_{\text{inj}}$. The proposed architecture is special because, under the ideal unitary model introduced next, it satisfies $P_{\text{rad}} = P_{\text{inj}}$ exactly.

We consider a narrowband multiuser downlink transmission to S single-antenna users. Let \mathbf{H} be the channel matrix, given by $\mathbf{H} = [\mathbf{h}_1, \dots, \mathbf{h}_S] \in \mathbb{C}^{N \times S}$, where \mathbf{h}_s is the channel to user s . Let y_s be the received signal at user s , and let \mathbf{y} denote the stacked received-signal vector. Then the received signal vector \mathbf{y} is given by

$$\mathbf{y} = \mathbf{H}^H \mathbf{F}_{\text{RF}} \mathbf{F}_{\text{BB}} \mathbf{s} + \mathbf{n}, \quad (6)$$

with $\mathbf{n} \sim \mathcal{CN}(\mathbf{0}, \sigma^2 \mathbf{I}_S)$.

Remark 1 (Interpretation of injected power and PA placement): In this work, $P_{\text{inj}} = \mathbb{E} \|\mathbf{x}\|_2^2$ models the total RF power delivered by the r RF-chains *after* their power amplifiers (PAs) into the input ports of the passive analog RF network. Equivalently, we assume that the analog RF network is a passive, lossless (in the ideal model) multiport driven by r high-power sources, while the

remaining $N - r$ input ports are terminated in matched loads. This setting captures architectures in which PAs are placed per RF-chain (centralized amplification). If instead amplification is distributed after the analog network (e.g., per-antenna PAs), then P_{inj} should be redefined at the PA outputs, and the equal-injected-power comparison in this paper would require a corresponding adjustment.

B. Lossless N -mode analog processor and excited inputs

We model the programmable analog beamformer as a lossless unitary N -mode linear RF processor acting on complex-envelope amplitudes, denoted by $\mathbf{X}(\Phi) \in \mathbb{C}^{N \times N}$, where Φ collects the programmable phase settings. Since the analog RF processor is unitary, it satisfies

$$\mathbf{X}(\Phi)^H \mathbf{X}(\Phi) = \mathbf{I}_N. \quad (7)$$

Now let $\mathbf{u}_{\text{in}} \in \mathbb{C}^{N \times 1}$ and $\mathbf{u}_{\text{out}} \in \mathbb{C}^{N \times 1}$ denote the complex amplitudes at the N input ports and the N output ports of the analog RF processor, respectively. Then the input–output relation is

$$\mathbf{u}_{\text{out}} = \mathbf{X}(\Phi) \mathbf{u}_{\text{in}}. \quad (8)$$

This is the ideal matched, lossless hardware model used in the paper. In an RF interpretation, $\mathbf{X}(\Phi)$ is the normalized transmission block of an N -port lossless network between the driven ports and the antenna ports. Moreover, note that \mathbf{u}_{out} is also the antenna-excitation vector.

Since there are only r RF-chains, only r out of the N input modes are driven by RF-chains, and the remaining $N - r$ inputs are terminated in matched loads, i.e., they have zero incident waves. Let $\mathbf{E}_r = [\mathbf{e}_1, \dots, \mathbf{e}_r] \in \mathbb{R}^{N \times r}$ embed the RF-chain vector $\mathbf{x} \in \mathbb{C}^r$ into \mathbb{C}^N via

$$\mathbf{u}_{\text{in}} = \mathbf{E}_r \mathbf{x}. \quad (9)$$

The antenna excitation is then

$$\mathbf{u}_{\text{out}} = \mathbf{X}(\Phi) \mathbf{E}_r \mathbf{x}, \quad (10)$$

so the analog beamformer is given by

$$\mathbf{F}_{\text{RF}}(\Phi) = \mathbf{X}(\Phi) \mathbf{E}_r \in \mathbb{C}^{N \times r}. \quad (11)$$

Because $\mathbf{X}(\Phi)$ is unitary, the analog beamformer is semi-unitary:

$$\mathbf{F}_{\text{RF}}(\Phi)^H \mathbf{F}_{\text{RF}}(\Phi) = \mathbf{I}_r. \quad (12)$$

Remark 2 (Notation convention): The analog beamformer is completely determined by the phase configuration Φ through (11). Accordingly, after (11) has been introduced we use \mathbf{F}_{RF} and $\mathbf{F}_{\text{RF}}(\Phi)$ interchangeably whenever the dependence on Φ is implicit. We write $\mathbf{F}_{\text{RF}}(\Phi)$ explicitly only when the optimization variable is the phase setting itself or when multiple phase configurations are being compared.

Proposition 1 (Power preservation of the proposed analog stage): For any $\mathbf{x} \in \mathbb{C}^r$, the analog beamformer in (11) preserves Euclidean norm:

$$\|\mathbf{F}_{\text{RF}}(\Phi)\mathbf{x}\|_2^2 = \|\mathbf{x}\|_2^2. \quad (13)$$

Consequently,

$$P_{\text{rad}} = P_{\text{inj}} \quad (14)$$

for the proposed architecture under the ideal unitary model.

Proof: Using (12),

$$\|\mathbf{F}_{\text{RF}}\mathbf{x}\|_2^2 = \mathbf{x}^H \mathbf{F}_{\text{RF}}^H \mathbf{F}_{\text{RF}} \mathbf{x} = \mathbf{x}^H \mathbf{x} = \|\mathbf{x}\|_2^2.$$

Taking expectation over $\mathbf{x} = \mathbf{F}_{\text{BBS}} \mathbf{g}$ gives $P_{\text{rad}} = P_{\text{inj}}$. ■

Remark 3 (Connection to lossless multiport networks): Under the standard power-wave (scattering) description of an N -port lossless network with matched terminations, the overall scattering matrix is unitary. In the ideal matched model used here, $\mathbf{X}(\Phi)$ can be interpreted as the effective transmission operator between the excited input waves and the antenna-port waves, normalized such that $\|\mathbf{u}\|_2^2$ equals total power. This justifies the unitary constraint $\mathbf{X}(\Phi)^H \mathbf{X}(\Phi) = \mathbf{I}_N$ as an idealization of a lossless, reflection-free network.

C. Realizing $\mathbf{X}(\Phi)$ via the interlaced mixer–phase architecture

We realize $\mathbf{X}(\Phi)$ as an interlaced product of a fixed unitary mixing layer $\mathbf{W} \in \mathbb{C}^{N \times N}$ and M programmable diagonal phase-shifting layers, as

$$\mathbf{X}(\Phi) = \mathbf{W} \mathbf{D}_M \mathbf{W} \mathbf{D}_{M-1} \cdots \mathbf{W} \mathbf{D}_1 \mathbf{W}, \quad (15)$$

where

$$\mathbf{D}_k(\phi_k) = \text{diag}(e^{j\phi_{1,k}}, \dots, e^{j\phi_{N,k}}) \quad (16)$$

and $\Phi = \{\phi_{n,k}\}$ collects all phases and represents the programmable phase setting. The fixed layer \mathbf{W} models a static coupler/splitter network or a fixed mixing medium and is assumed to

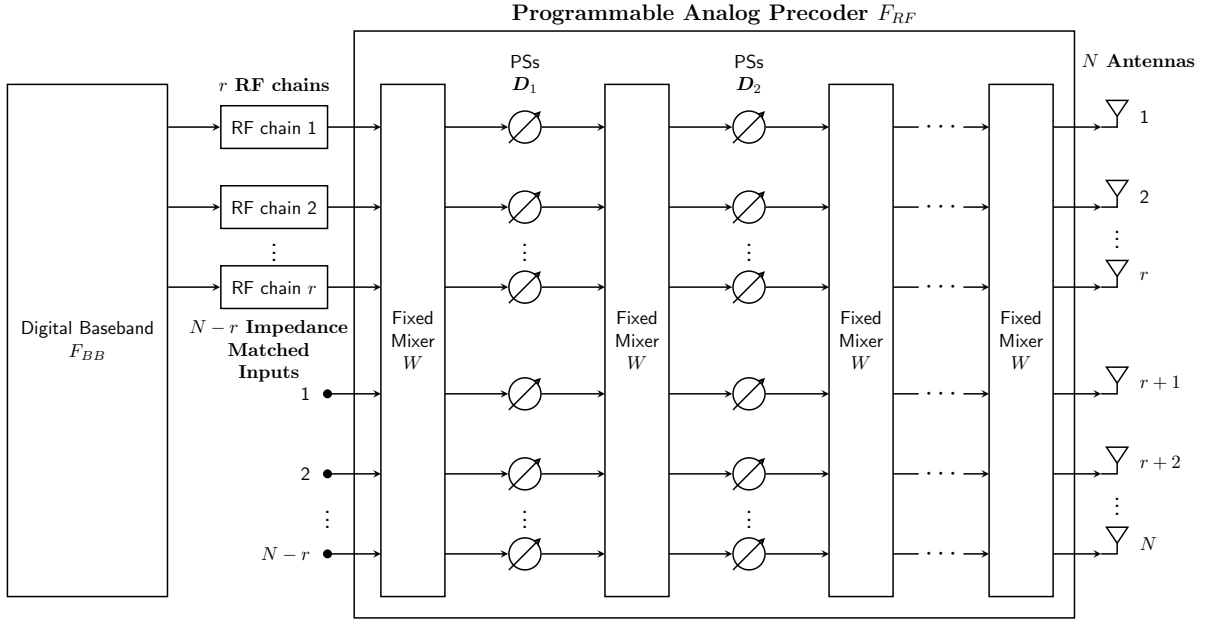


Fig. 1. System diagram of the proposed hybrid transmitter with an interlaced programmable unitary RF network. The analog stage is the first r columns of an $N \times N$ programmable unitary processor.

be sufficiently mixing, consistent with [7], [8]. Because each factor in (15) is unitary, the overall processor $\mathbf{X}(\Phi)$ remains unitary for every phase configuration.

D. End-to-end transmitter architecture

As explained in Section II-B, the analog beamformer \mathbf{F}_{RF} is realized via the unitary analog RF processor modeled via the matrix $\mathbf{X}(\Phi)$, when only r out of the N input modes are driven by RF-chains, and the remaining $N - r$ inputs are terminated in matched loads. Next, as explained in Section II-C, the unitary analog RF processor, $\mathbf{X}(\Phi)$, is realized as a cascade of unitary mixing layers interlaced by programmable diagonal phase-shifting layers, as in (15). Combining all of this, along with the digital beamformer and the N antennas, a realizable hardware model of the hybrid beamforming architecture is shown in Figure 1.

As can be seen from Figure 1, the digital beamformer \mathbf{F}_{BB} produces the vector \mathbf{x} in (2). The entries of \mathbf{x} are upconverted by the r RF-chains and injected into the first r inputs of the programmable analog beamformer $\mathbf{F}_{\text{RF}}(\Phi)$, while the remaining $N - r$ inputs are terminated in matched loads. The phase settings Φ program the analog beamformer so that the resulting

antenna excitation

$$\mathbf{x}_{\text{ant}} = \mathbf{F}_{\text{RF}}(\Phi)\mathbf{x}$$

approximates the desired fully-digital excitation vector.

E. Problem Formulation

Let $\mathbf{F}_{\text{tar}} \in \mathbb{C}^{N \times S}$ denote a target matrix whose columns span the desired S -dimensional transmit subspace, e.g., an orthonormal basis extracted from a fully-digital precoder or from a channel factorization. We approximate \mathbf{F}_{tar} via the composite hybrid beamformer $\mathbf{F}_{\text{RF}}\mathbf{F}_{\text{BB}}$ by solving the following optimization problem

$$\min_{\mathbf{F}_{\text{RF}}, \mathbf{F}_{\text{BB}}} \left\| \mathbf{F}_{\text{tar}} - \mathbf{F}_{\text{RF}}\mathbf{F}_{\text{BB}} \right\|_F^2, \quad (17)$$

subject to the analog realizability constraints induced by (11)–(15). Due to these constraints, the optimization of \mathbf{F}_{RF} is done only via the optimization of the phase-shifters of the diagonal matrices in (15). The optimization of \mathbf{F}_{BB} is unconstrained.

F. Closed-form digital beamformer and reduced objective

For fixed Φ , (17) is least squares in \mathbf{F}_{BB} with minimizer $\mathbf{F}_{\text{BB}}^* = (\mathbf{F}_{\text{RF}}^H \mathbf{F}_{\text{RF}})^{-1} \mathbf{F}_{\text{RF}}^H \mathbf{F}_{\text{tar}}$. Because the proposed analog beamformer is semi-unitary, $\mathbf{F}_{\text{RF}}^H \mathbf{F}_{\text{RF}} = \mathbf{I}_r$ by (12), the solution of (17) simplifies to

$$\mathbf{F}_{\text{BB}}^* = \mathbf{F}_{\text{RF}}(\Phi)^H \mathbf{F}_{\text{tar}}. \quad (18)$$

Substituting (18) into (1) yields

$$\mathbf{F}(\Phi) = \mathbf{F}_{\text{RF}}(\Phi)\mathbf{F}_{\text{RF}}(\Phi)^H \mathbf{F}_{\text{tar}} = \mathbf{\Pi}(\Phi)\mathbf{F}_{\text{tar}}, \quad (19)$$

where

$$\mathbf{\Pi}(\Phi) \triangleq \mathbf{F}_{\text{RF}}(\Phi)\mathbf{F}_{\text{RF}}(\Phi)^H \quad (20)$$

is the projector onto the realizable analog subspace $\mathcal{V}_r(\Phi) = \text{range}(\mathbf{F}_{\text{RF}}(\Phi))$.

Moreover, inserting (18) into the main optimization problem (17) yields

$$\begin{aligned} \min_{\mathbf{F}_{\text{BB}}, \mathbf{F}_{\text{RF}}(\Phi)} \left\| \mathbf{F}_{\text{tar}} - \mathbf{F}_{\text{RF}}(\Phi)\mathbf{F}_{\text{BB}} \right\|_F^2 \\ = \left\| \mathbf{F}_{\text{tar}} \right\|_F^2 - \max_{\mathbf{F}_{\text{RF}}(\Phi)} \left\| \mathbf{F}_{\text{tar}}^H \mathbf{F}_{\text{RF}}(\Phi) \right\|_F^2. \end{aligned} \quad (21)$$

Hence, the programming of the analog beamformer, via the phase-shifters of the diagonal matrices in (15), such that the objective in (17) is minimized reduces to

$$\Phi^* = \arg \max_{\Phi} \|\mathbf{F}_{\text{tar}}^H \mathbf{F}_{\text{RF}}(\Phi)\|_F^2. \quad (22)$$

The reduced objective (22) is valid for any matrix $\mathbf{F}_{\text{tar}} \in \mathbb{C}^{N \times S}$. When \mathbf{F}_{tar} has orthonormal columns, the objective depends only on the target subspace and admits a principal-angle and chordal-distance interpretation. When \mathbf{F}_{tar} is not column-orthonormal, (22) should be interpreted as matching an energy-weighted target matrix rather than a pure subspace.

Corollary 1 (Exact recovery under subspace containment): Assume $S \leq r$ and

$$\text{range}(\mathbf{F}_{\text{tar}}) \subseteq \text{range}(\mathbf{F}_{\text{RF}}(\Phi)). \quad (23)$$

Then the digital matrix in (18) satisfies

$$\mathbf{F}_{\text{RF}}(\Phi) \mathbf{F}_{\text{BB}}^* = \mathbf{F}_{\text{tar}} \quad (24)$$

and

$$\|\mathbf{F}_{\text{BB}}^*\|_F^2 = \|\mathbf{F}_{\text{tar}}\|_F^2. \quad (25)$$

Thus, exact hybrid recovery is achieved with the same injected power as the target fully-digital precoder.

Proof: The containment condition implies that $\mathbf{\Pi}(\Phi)$ acts as the identity on $\text{range}(\mathbf{F}_{\text{tar}})$; hence (19) gives $\mathbf{F}_{\text{RF}} \mathbf{F}_{\text{BB}}^* = \mathbf{F}_{\text{tar}}$. Also,

$$\|\mathbf{F}_{\text{BB}}^*\|_F^2 = \|\mathbf{F}_{\text{RF}}^H \mathbf{F}_{\text{tar}}\|_F^2 = \text{tr}(\mathbf{F}_{\text{tar}}^H \mathbf{F}_{\text{RF}} \mathbf{F}_{\text{RF}}^H \mathbf{F}_{\text{tar}}) = \|\mathbf{F}_{\text{tar}}\|_F^2. \quad \blacksquare$$

G. Phase programming via adjoint gradients

Having derived the optimal digital beamformer, we are left to determine Φ^* by solving (22). In other words, we optimize the phase-shifters of the analog beamformer so that the composite hybrid beamformer $\mathbf{F}_{\text{RF}} \mathbf{F}_{\text{BB}}$ approximates the fully-digital target \mathbf{F}_{tar} .

The optimization problem in (22), under the constraints of (11) and (15), is nonconvex. Here we do not seek its global optimum; instead, we use a practical suboptimal solution based on gradient descent, as described below.

Using the objective in (22) and the real-differential convention $d\mathcal{L} = \Re\{\text{tr}(\mathbf{G}^H d\mathbf{F}_{\text{RF}})\}$ for

$$\mathcal{L}(\Phi) \triangleq -\|\mathbf{F}_{\text{tar}}^H \mathbf{F}_{\text{RF}}(\Phi)\|_F^2, \quad (26)$$

the Euclidean gradient with respect to \mathbf{F}_{RF} is

$$\mathbf{G} = -2 \mathbf{F}_{\text{tar}} (\mathbf{F}_{\text{tar}}^H \mathbf{F}_{\text{RF}}). \quad (27)$$

Forward pass: set $\mathbf{Z}_0 = \mathbf{W}\mathbf{E}_r$ and for $k = 1, \dots, M$ compute

$$\mathbf{B}_k = \mathbf{Z}_{k-1}, \quad \mathbf{Z}_k = \mathbf{W}\mathbf{D}_k \mathbf{Z}_{k-1}, \quad (28)$$

so that $\mathbf{F}_{\text{RF}} = \mathbf{Z}_M$.

Backward pass: set $\mathbf{Y}_{M+1} = \mathbf{G}$ and for $k = M, \dots, 1$ compute

$$\mathbf{A}_k = \mathbf{W}^H \mathbf{Y}_{k+1}, \quad \mathbf{Y}_k = \mathbf{D}_k^H \mathbf{A}_k, \quad (29)$$

and form the phase gradient

$$\nabla_{\phi_k} \mathcal{L} = \Im \left\{ \left((\mathbf{A}_k \odot \mathbf{B}_k^*) \mathbf{1}_r \right) \odot e^{-j\phi_k} \right\}. \quad (30)$$

Since $\mathbf{Z}_0 = \mathbf{W}\mathbf{E}_r$ does not depend on Φ , it can be precomputed once. When the matrix \mathbf{W} is a DFT matrix, i.e., for a DFT mixer, each iteration uses M multiplications by \mathbf{W} and M multiplications by \mathbf{W}^H , yielding $\mathcal{O}(MrN \log N)$ complexity. We use $(\cdot)^*$ for elementwise conjugation, $(\cdot)^H$ for the Hermitian transpose, and \odot for the Hadamard product.

Gauge fixing: one global phase per layer does not affect (22); we therefore fix $\phi_{1,k} = 0$ and set the corresponding gradient entry to zero.

H. Programming algorithm

Using (28)–(30), the phase-shifters can be updated by any first-order optimizer on the phase torus (e.g., gradient descent or Adam). Algorithm 1 summarizes the required forward/backward passes and gradient computation; the specific optimizer update rule can be chosen based on implementation needs.

Equation (22) is nonconvex. In the numerical study, for each depth M we therefore run Algorithm 1 from a small number of independent random initializations and retain the continuous-phase candidate that maximizes the analog subspace score $\|\mathbf{F}_{\text{tar}}^H \mathbf{F}_{\text{RF}}(\Phi)\|_F^2$. Each depth is optimized independently rather than warm-started from a neighboring depth.

Algorithm 1 Adjoint-gradient computation for interlaced mixer–phase programming (used with GD/Adam updates)

- 1: **Input:** Target \mathbf{F}_{tar} , antennas N , RF-chains r , streams S , layers M , step size η .
 - 2: Initialize fixed mixer \mathbf{W} and phases Φ (e.g., i.i.d. uniform in $[0, 2\pi)$); enforce gauge $\phi_{1,k} = 0$.
 - 3: Precompute $\mathbf{Z}_0 = \mathbf{W}\mathbf{E}_r$.
 - 4: **while** not converged **do**
 - 5: **Forward:** set \mathbf{Z}_0 to the precomputed value; for $k = 1$ to M : store $\mathbf{B}_k = \mathbf{Z}_{k-1}$ and update $\mathbf{Z}_k = \mathbf{W}\mathbf{D}_k\mathbf{Z}_{k-1}$.
 - 6: Set $\mathbf{F}_{\text{RF}} = \mathbf{Z}_M$ and compute $\mathbf{T} = \mathbf{F}_{\text{tar}}^H \mathbf{F}_{\text{RF}}$.
 - 7: **Seed gradient:** compute $\mathbf{G} = -2 \mathbf{F}_{\text{tar}} \mathbf{T}$.
 - 8: **Backward:** set $\mathbf{Y}_{M+1} = \mathbf{G}$; for $k = M$ down to 1:
 - 9: compute $\mathbf{A}_k = \mathbf{W}^H \mathbf{Y}_{k+1}$ and $\mathbf{Y}_k = \mathbf{D}_k^H \mathbf{A}_k$;
 - 10: compute $\nabla_{\phi_k} \mathcal{L}$ via (30) and set $[\nabla_{\phi_k} \mathcal{L}]_1 = 0$.
 - 11: **Update:** $\phi_k \leftarrow \phi_k - \eta \nabla_{\phi_k} \mathcal{L}$ for all k .
 - 12: **end while**
 - 13: **Output:** The phase-settings Φ of \mathbf{F}_{RF} .
-

I. MMSE specialization used in the numerical study

The formulation in (17)–(22) is target-agnostic and applies to an arbitrary matrix \mathbf{F}_{tar} . In the numerical study, however, performance is evaluated with an MMSE digital precoder after the analog subspace has been programmed. For this reason, we now specialize the general framework to the case in which the programmed analog subspace contains the channel subspace and the digital stage is recomputed from the effective channel. The following corollary explains when this hybrid MMSE construction coincides exactly with the fully-digital MMSE precoder.

Corollary 2 (MMSE equivalence under channel-subspace containment): Assume $\text{rank}(\mathbf{H}) = S \leq r$ and

$$\text{range}(\mathbf{H}) \subseteq \text{range}(\mathbf{F}_{\text{RF}}(\Phi)). \quad (31)$$

Let

$$\mathbf{G} \triangleq \mathbf{F}_{\text{RF}}(\Phi)^H \mathbf{H} \in \mathbb{C}^{r \times S}, \quad (32)$$

so that $\mathbf{H} = \mathbf{F}_{\text{RF}}(\Phi)\mathbf{G}$. Define the unnormalized fully-digital MMSE precoder

$$\tilde{\mathbf{F}}_{\text{FD}} = \mathbf{H} (\mathbf{H}^H \mathbf{H} + \alpha \mathbf{I}_S)^{-1}, \quad \alpha > 0, \quad (33)$$

and define the effective channel

$$\mathbf{H}_{\text{eff}} = \mathbf{H}^H \mathbf{F}_{\text{RF}}(\Phi). \quad (34)$$

The unnormalized hybrid MMSE precoder is

$$\tilde{\mathbf{F}}_{\text{HYB}} = \mathbf{F}_{\text{RF}}(\Phi) \mathbf{H}_{\text{eff}}^H (\mathbf{H}_{\text{eff}} \mathbf{H}_{\text{eff}}^H + \alpha \mathbf{I}_S)^{-1}. \quad (35)$$

Then

$$\tilde{\mathbf{F}}_{\text{HYB}} = \tilde{\mathbf{F}}_{\text{FD}}. \quad (36)$$

After Frobenius normalization to the same injected power P_T , the two precoders remain identical.

Proof: Since $\mathbf{F}_{\text{RF}}^H \mathbf{F}_{\text{RF}} = \mathbf{I}_r$ and $\text{range}(\mathbf{H}) \subseteq \text{range}(\mathbf{F}_{\text{RF}})$, we have $\mathbf{H} = \mathbf{F}_{\text{RF}} \mathbf{G}$ with $\mathbf{G} = \mathbf{F}_{\text{RF}}^H \mathbf{H}$. Hence

$$\mathbf{H}_{\text{eff}} = \mathbf{H}^H \mathbf{F}_{\text{RF}} = \mathbf{G}^H \quad (37)$$

and

$$\mathbf{H}^H \mathbf{H} = \mathbf{G}^H \mathbf{F}_{\text{RF}}^H \mathbf{F}_{\text{RF}} \mathbf{G} = \mathbf{G}^H \mathbf{G}. \quad (38)$$

Therefore,

$$\begin{aligned} \tilde{\mathbf{F}}_{\text{HYB}} &= \mathbf{F}_{\text{RF}} \mathbf{G} (\mathbf{G}^H \mathbf{G} + \alpha \mathbf{I}_S)^{-1} \\ &= \mathbf{H} (\mathbf{H}^H \mathbf{H} + \alpha \mathbf{I}_S)^{-1} = \tilde{\mathbf{F}}_{\text{FD}}. \end{aligned} \quad (39)$$

The same Frobenius normalization then preserves equality. ■

Corollary 2 explains the numerical setup in Section VI: programming the analog stage against an orthonormal basis of $\text{range}(\mathbf{H})$ and then recomputing the digital MMSE stage over the effective channel exactly reproduces the fully-digital MMSE precoder whenever the programmed analog subspace contains the channel subspace.

III. PHASE-QUANTIZED PROGRAMMING UNDER EQUAL INJECTED POWER

Practical programmable phase layers provide finite resolution. Following [7], we model each phase element as a q -bit variable

$$\phi_{n,k} \in \mathcal{Q}_q \triangleq \{0, \Delta, 2\Delta, \dots, (2^q - 1)\Delta\}, \quad \Delta \triangleq \frac{2\pi}{2^q}. \quad (40)$$

Let $Q_q(\cdot)$ denote wrapping quantization to \mathcal{Q}_q modulo 2π , applied elementwise. Starting from the continuous-phase solution Φ^{cont} , we form

$$\Phi^{(q)} = Q_q(\Phi^{\text{cont}}) \quad (41)$$

and the corresponding quantized analog beamformer

$$\mathbf{F}_{\text{RF}}^{(q)} = \mathbf{F}_{\text{RF}}(\Phi^{(q)}). \quad (42)$$

Remark 4 (Quantization preserves RF efficiency): Because every quantized diagonal layer $\mathbf{D}_k(\phi_k^{(q)})$ remains unitary, the full processor $\mathbf{X}(\Phi^{(q)})$ is still unitary and

$$(\mathbf{F}_{\text{RF}}^{(q)})^H \mathbf{F}_{\text{RF}}^{(q)} = \mathbf{I}_r. \quad (43)$$

Hence, under the injected-power normalization

$$\|\mathbf{F}_{\text{BB}}^{(q)}\|_F^2 = P_T, \quad (44)$$

the quantized architecture remains exactly power-preserving:

$$\|\mathbf{F}_{\text{RF}}^{(q)} \mathbf{F}_{\text{BB}}^{(q)}\|_F^2 = P_T. \quad (45)$$

Therefore, phase quantization affects only the reachable analog subspace and not the RF transfer efficiency.

A. Practical quantized programming

For a fixed channel realization and depth M , we solve the continuous-phase problem (22) from N_{rst} independent random initializations, which produces a pool of continuous-phase candidates. The continuous-phase design is the candidate in this pool with the largest subspace score

$$\|\mathbf{F}_{\text{tar}}^H \mathbf{F}_{\text{RF}}(\Phi)\|_F^2. \quad (46)$$

For each quantization level q , every candidate in the same restart pool is then quantized elementwise,

$$\Phi^{(q)} = Q_q(\Phi^{\text{cont}}), \quad (47)$$

while preserving the per-layer gauge $\phi_{1,k} = 0$, and is subsequently refined by a greedy local discrete search on the quantized phase grid. Specifically, letting

$$\Delta = \frac{2\pi}{2^q}, \quad (48)$$

each phase entry is updated over the candidate set

$$\{\phi, \phi + \Delta, \phi - \Delta\} \pmod{2\pi} \quad (49)$$

for a small number of refinement sweeps. The final q -bit analog beamformer is the refined quantized candidate with the largest subspace score among the same restart pool:

$$\mathbf{F}_{\text{RF}}^{(q)} = \mathbf{F}_{\text{RF}}(\Phi_{\text{best}}^{(q)}). \quad (50)$$

Thus, the best q -bit design is selected independently of the best continuous-phase design.

The quantized analog design itself remains target-agnostic. For any prescribed target matrix \mathbf{F}_{tar} , the continuous-phase candidates are quantized and refined so as to maximize the same score

$$\|\mathbf{F}_{\text{tar}}^H \mathbf{F}_{\text{RF}}(\Phi)\|_F^2, \quad (51)$$

which is the discrete counterpart of the generic objective in (22). Only after the quantized analog matrix has been fixed do we specialize the digital stage to the communication criterion used for evaluation.

B. MMSE specialization used in the numerical study

In the numerical study we evaluate rates with an MMSE digital precoder. Accordingly, after the analog stage is fixed, we recompute the digital MMSE stage over the effective channel

$$\mathbf{H}_{\text{eff}}^{(q)} = \mathbf{H}^H \mathbf{F}_{\text{RF}}^{(q)}. \quad (52)$$

Specifically, we form

$$\tilde{\mathbf{F}}_{\text{BB}}^{(q)} = (\mathbf{H}_{\text{eff}}^{(q)})^H \left(\mathbf{H}_{\text{eff}}^{(q)} (\mathbf{H}_{\text{eff}}^{(q)})^H + \frac{S\sigma^2}{P_T} \mathbf{I}_S \right)^{-1} \quad (53)$$

and scale it by a real factor α_q so that

$$\mathbf{F}_{\text{BB}}^{(q)} = \alpha_q \tilde{\mathbf{F}}_{\text{BB}}^{(q)}, \quad \|\mathbf{F}_{\text{BB}}^{(q)}\|_F^2 = P_T. \quad (54)$$

Thus, phase quantization changes only the realizable analog subspace. In the present numerical setup, the subsequent digital-stage update is MMSE-specific, whereas the quantized analog programming itself is still driven by the general target-matching objective.

IV. STREAM-AWARE DEPTH SCALING AND COMPLEXITY ANALYSIS

The hybrid precoder in (19) depends on the analog network only through the rank- r projector $\mathbf{\Pi}(\Phi)$, i.e., through the realizable r -dimensional subspace $\mathcal{V}_r(\Phi) = \text{range}(\mathbf{F}_{\text{RF}}(\Phi))$. Therefore, the natural design space is the complex Grassmann manifold

$$\text{Gr}(r, N) \triangleq \{r\text{-dimensional subspaces of } \mathbb{C}^N\}, \quad (55)$$

whose real dimension is $\dim \text{Gr}(r, N) = 2r(N - r)$.

A. Geometry induced by S streams

Let $\mathcal{U}_S \triangleq \text{range}(\mathbf{F}_{\text{tar}}) \subset \mathbb{C}^N$ denote the desired S -dimensional signal subspace. The hybrid architecture with $r \geq S$ can represent \mathbf{F}_{tar} exactly whenever

$$\mathcal{U}_S \subseteq \mathcal{V}_r(\Phi), \quad (56)$$

because then the projector $\mathbf{\Pi}(\Phi)$ acts as the identity on \mathcal{U}_S .

For a fixed target \mathcal{U}_S , the set of r -subspaces that contain it is

$$\mathcal{C}(\mathcal{U}_S) \triangleq \{\mathcal{V}_r \in \text{Gr}(r, N) : \mathcal{U}_S \subseteq \mathcal{V}_r\}, \quad (57)$$

and satisfies $\mathcal{C}(\mathcal{U}_S) \cong \text{Gr}(r - S, N - S)$ with dimension

$$\dim \mathcal{C}(\mathcal{U}_S) = 2(r - S)(N - r). \quad (58)$$

Thus, the containment constraint (56) has codimension $2S(N - r)$ inside $\text{Gr}(r, N)$.

B. Controllable degrees of freedom and a depth guideline

The interlaced network uses M diagonal phase layers, each with N tunable phases. One global phase per layer is redundant for the induced subspace and for the objective in (22), leaving approximately

$$k_{\text{ctrl}} \approx M(N - 1) \quad (59)$$

effective real control parameters.

Proposition 2 (Stream-aware DoF guideline (dimension-counting, necessary)): Assume $r \geq S$ and consider the worst-case requirement that, for an arbitrary S -dimensional signal subspace $\mathcal{U}_S \subset \mathbb{C}^N$, there exists a phase setting Φ such that the realizable analog subspace $\mathcal{V}_r(\Phi)$ satisfies $\mathcal{U}_S \subseteq \mathcal{V}_r(\Phi)$. A necessary (dimension-counting) condition for this to hold generically is $k_{\text{ctrl}} \gtrsim 2S(N - r)$, which implies

$$M \gtrsim \left\lceil \frac{2S(N - r)}{N - 1} \right\rceil. \quad (60)$$

Proof sketch: This is a dimension-counting heuristic under generic regularity/transversality assumptions on the map $\Phi \mapsto \mathcal{V}_r(\Phi)$; it is a necessary guideline, not a sufficiency result. The phase parameters live on an MN -dimensional real torus. For any layer k , adding a constant offset to all N phases multiplies \mathbf{D}_k by a unit-modulus scalar and hence scales $\mathbf{X}(\Phi)$ and \mathbf{F}_{RF} by a global phase, which leaves the induced subspace and (22) unchanged. Thus, at most

$k_{\text{ctrl}} = M(N-1)$ independent real directions can affect the objective/subspace. For a fixed \mathcal{U}_S , the containment set $\mathcal{C}(\mathcal{U}_S)$ has codimension $2S(N-r)$ in $\text{Gr}(r, N)$ by (58). A generic k_{ctrl} -parameter family can intersect an arbitrary codimension- $2S(N-r)$ subset only if $k_{\text{ctrl}} \geq 2S(N-r)$, yielding (60). \blacksquare

Remark 5 (Interpretation and limitations): The guideline (60) links network depth primarily to (S, r) rather than to N . (i) If $r = S$, then $M \gtrsim \left\lceil \frac{2S(N-S)}{N-1} \right\rceil \approx 2S$ for $N \gg S$. (ii) If $S < r < N$, the required M decreases with r , reflecting increased slack in choosing an r -subspace that contains a fixed S -subspace. (iii) The bound is necessary but not sufficient: coverage also depends on the differential properties of the map $\Phi \mapsto \mathcal{V}_r(\Phi)$ induced by (15). Finally, the reachable subspace dimension cannot exceed $\min\{M(N-1), 2r(N-r)\}$, so once $M(N-1) \gtrsim 2r(N-r)$, additional layers can improve conditioning and optimization landscape but not the local dimension of the reachable set. Moreover, Proposition 2 provides a dimension-counting necessary guideline for generic subspace containment. It does not, by itself, prove that a given depth M is sufficient for exact hybrid recovery. Exact recovery follows only when the realized analog subspace satisfies

$$\text{range}(\mathbf{F}_{\text{tar}}) \subseteq \text{range}(\mathbf{F}_{\text{RF}}(\Phi)),$$

as stated in Corollary 1. Accordingly, in the numerical section we interpret $M \approx 2S$ as a practical design guideline rather than as a formal sufficiency threshold.

V. COMPARATOR BASELINES UNDER EQUAL INJECTED POWER

This section specifies the three comparator architectures used in the numerical study. The comparison is intentionally performed at equal *injected* power P_T , not at equal radiated power. For every hybrid architecture,

$$P_T = \|\mathbf{F}_{\text{BB}}\|_F^2 \tag{61}$$

is fixed, while the radiated power is

$$P_{\text{rad}} = \|\mathbf{F}_{\text{RF}}\mathbf{F}_{\text{BB}}\|_F^2 = \eta_{\text{RF}}P_T, \tag{62}$$

where

$$\eta_{\text{RF}} \triangleq \frac{\|\mathbf{F}_{\text{RF}}\mathbf{F}_{\text{BB}}\|_F^2}{\|\mathbf{F}_{\text{BB}}\|_F^2} \tag{63}$$

is the RF transfer efficiency. For the proposed unitary RF-network architecture, Proposition 1 gives $\eta_{\text{RF}} = 1$. For the fully-connected hybrid beamforming architectures in [3] and [4], which

we use as baseline, the transfer efficiency is $0 < \eta_{\text{RF}} < 1$. For the ideal-lossless Butler/DFT beam-selection baseline of Subsection V-C, the RF stage is a selected submatrix of a unitary DFT transform and therefore also satisfies $\eta_{\text{RF}} = 1$.

A. Sohrabi–Yu fully-connected baseline

The Sohrabi–Yu fully-connected hybrid beamforming architecture (FC1) in [3] uses one phase-shifter per RF-chain to antenna connection. It is chosen as a baseline since this architecture is the most widely adopted and studied hybrid beamforming architecture.

FC1 in [3] uses an abstract fully-connected analog matrix $\tilde{\mathbf{F}}_{\text{RF}}^{\text{FC1}} \in \mathbb{C}^{N \times r_{\text{FC1}}}$ with unit-modulus entries. In the exact-representation regime of Proposition 2 in [3], one uses $r_{\text{FC1}} = 2S$ RF-chains and continuous phases to factor a target matrix \mathbf{F}_{tar} as

$$\mathbf{F}_{\text{tar}} = \tilde{\mathbf{F}}_{\text{RF}}^{\text{FC1}} \tilde{\mathbf{F}}_{\text{BB}}^{\text{FC1}} \quad (64)$$

under the *abstract* model.

To compare on a physical footing, we realize the FC1 network as an ideal passive splitter–phase-shifter–combiner network. The resulting transfer from the RF-chain outputs to the antenna ports is

$$\mathbf{F}_{\text{RF}}^{\text{FC1}} = \frac{1}{\sqrt{Nr_{\text{FC1}}}} \tilde{\mathbf{F}}_{\text{RF}}^{\text{FC1}}. \quad (65)$$

The factor $1/\sqrt{N}$ accounts for equal splitting of each RF-chain signal into N branches, while $1/\sqrt{r_{\text{FC1}}}$ accounts for ideal equal-power combining of r_{FC1} branches at each antenna port. Hence $\|\mathbf{F}_{\text{RF}}^{\text{FC1}}\|_2 \leq 1$, and therefore the physical FC1 transfer is contractive.

In the numerical evaluation, $\tilde{\mathbf{F}}_{\text{RF}}^{\text{FC1}}$ is first constructed from \mathbf{F}_{tar} using the continuous-phase exact-representation rule of [3] and then interpreted through the passive transfer (65). Once the physical analog matrix is fixed, the digital stage is recomputed over the effective channel

$$\mathbf{H}_{\text{eff}}^{\text{FC1}} = \mathbf{H}^H \mathbf{F}_{\text{RF}}^{\text{FC1}} \quad (66)$$

using the same MMSE rule as for the proposed architecture, followed by scaling to satisfy

$$\|\mathbf{F}_{\text{BB}}^{\text{FC1}}\|_F^2 = P_T. \quad (67)$$

Hence the FC1 baseline is evaluated under the same injected-power normalization as the proposed architecture, while its radiated power is reduced by the contractive physical RF transfer.

B. Yu–Zhang–Letaief fully-connected baseline

The Yu–Zhang–Letaief fully-connected two-phase-shifter (FC2) architecture in [4] uses two phase-shifters per RF-chain-to-antenna connection. It is chosen as a baseline because, under equal-radiated-power normalization and in the narrowband case with $r = S$, it can match the performance of the fully-digital architecture. As the numerical results in this paper show, however, its performance is much weaker under equal injected power because the physical RF transfer is contractive.

The abstract RF matrix of FC2 is given by

$$\tilde{\mathbf{F}}_{\text{RF}}^{\text{FC2}} = \Phi_1 + \Phi_2, \quad (68)$$

where $\Phi_1, \Phi_2 \in \mathbb{C}^{N \times r}$ have unit-modulus entries.

For the physical passive implementation, each RF-chain signal is split into $2N$ branches and each antenna port combines $2r$ branches. The corresponding transfer matrix is

$$\mathbf{F}_{\text{RF}}^{\text{FC2}} = \frac{1}{2\sqrt{Nr}} (\Phi_1 + \Phi_2), \quad (69)$$

which is again contractive.

In our physically fair baseline, let the target matrix have compact SVD

$$\mathbf{F}_{\text{tar}} = \mathbf{U}\Sigma\mathbf{V}^H. \quad (70)$$

We construct the largest columnwise-scaled passive FC2 analog stage

$$\mathbf{F}_{\text{RF}}^{\text{FC2}} = \mathbf{U}\mathbf{D}, \quad (71)$$

where

$$\mathbf{D} = \text{diag}(d_1, \dots, d_r), \quad d_j = \frac{1}{\sqrt{Nr} \max_i |U_{ij}|}, \quad (72)$$

so that every entry of $\mathbf{U}\mathbf{D}$ is exactly realizable by the passive FC2 network in (69).

In the numerical evaluation, the physically realizable analog matrix $\mathbf{F}_{\text{RF}}^{\text{FC2}} = \mathbf{U}\mathbf{D}$ is fixed first, and the digital stage is then recomputed over the corresponding effective channel

$$\mathbf{H}_{\text{eff}}^{\text{FC2}} = \mathbf{H}^H \mathbf{F}_{\text{RF}}^{\text{FC2}} \quad (73)$$

using the same MMSE rule as for the proposed architecture, followed by scaling to satisfy

$$\|\mathbf{F}_{\text{BB}}^{\text{FC2}}\|_F^2 = P_T. \quad (74)$$

Thus, the FC2 baseline preserves the target subspace through its analog design, but its end-to-end rate under equal injected power is evaluated through the actual effective channel induced by the contractive physical RF transfer.

Remark 6 (RF-chain count and comparison axes): Some architectures (e.g., FC1 in [3]) require a larger number of RF-chains (here $r_{\text{FC1}} = 2S$) to guarantee exact factorization under the abstract constant-modulus model. In this paper we compare architectures under a fixed *total injected RF power* budget P_T , i.e., the total power delivered by all RF-chains after their PAs is held constant. Thus, when an architecture uses more RF-chains, the available injected power is distributed across more chains, and the architecture also implicitly incurs additional RF-chain hardware (PAs, mixers, DACs, routing). Accordingly, the present comparison should be interpreted as equal total post-PA injected power and equal propagation conditions, but not as equal RF-chain count or equal hardware complexity.

C. Ideal-lossless Garcia-inspired Butler/DFT beam-selection baseline

Inspired by the DFT/Butler ABFN model of [2], we consider its ideal-lossless limit, in which the RF stage is restricted to beam selection within a fixed Fourier basis. Unlike the full realistic model in [2], which includes multiplicative loss factors from the hybrid couplers and phase-shifters, the present baseline deliberately omits static insertion loss in order to isolate fixed-basis, non-contractive RF transport from analog-subspace programmability.

Let

$$\mathbf{U}_{\text{DFT}} \in \mathbb{C}^{N \times N} \quad (75)$$

denote the unitary DFT matrix and let

$$\mathbf{F}_{\text{RF}}^{\text{BM}} = \mathbf{U}_{\text{DFT}} \mathbf{E}_{\mathcal{B}} \in \mathbb{C}^{N \times r_{\text{BM}}}, \quad (76)$$

where $\mathbf{E}_{\mathcal{B}}$ selects the columns indexed by $\mathcal{B} \subseteq \{1, \dots, N\}$ with $|\mathcal{B}| = r_{\text{BM}}$. Because \mathbf{U}_{DFT} is unitary, the selected-beam analog matrix is semi-unitary:

$$(\mathbf{F}_{\text{RF}}^{\text{BM}})^H \mathbf{F}_{\text{RF}}^{\text{BM}} = \mathbf{I}_{r_{\text{BM}}}, \quad (77)$$

and therefore preserves injected power under the same ideal matched model used for the proposed architecture.

To make the baseline as competitive as possible within its fixed Fourier basis, we choose the beam set \mathcal{B} adaptively for each channel realization using the same target subspace \mathbf{F}_{tar} . Let \mathbf{u}_n denote the n -th column of \mathbf{U}_{DFT} and define

$$c_n \triangleq \|\mathbf{F}_{\text{tar}}^H \mathbf{u}_n\|_2^2, \quad n = 1, \dots, N. \quad (78)$$

We then select the r_{BM} indices with the largest values of c_n . Since the DFT columns are orthonormal, this rule maximizes

$$\|\mathbf{F}_{\text{tar}}^H \mathbf{F}_{\text{RF}}^{\text{BM}}\|_F^2 \quad (79)$$

over all size- r_{BM} subsets of DFT beams.

Note that in this architecture, \mathbf{U}_{DFT} is fixed; only the selection matrix $\mathbf{E}_{\mathcal{B}}$ is allowed to depend on the channel realization. Thus, this baseline models an ideal adaptive beam selector operating on top of a fixed Butler/DFT codebook. It is only achievable if switching between ports can track the channel realization itself. By contrast, the beam-selection mechanism in [2] adapts on the much slower covariance timescale. Hence, the baseline considered here is deliberately optimistic and can be interpreted as an upper bound on the covariance-based DFT beam allocation of [2].

This target-matched beam-selection rule is used here as a favorable fixed-basis reference; it is not intended as an exact reproduction of the covariance-based beam-selection rule used in [2].

After fixing $\mathbf{F}_{\text{RF}}^{\text{BM}}$, we recompute the digital MMSE stage over the effective channel

$$\mathbf{H}_{\text{eff}}^{\text{BM}} = \mathbf{H}^H \mathbf{F}_{\text{RF}}^{\text{BM}} \quad (80)$$

using the same rule as for the proposed architecture, and scale it so that

$$\|\mathbf{F}_{\text{BB}}^{\text{BM}}\|_F^2 = P_T. \quad (81)$$

Hence the Butler/DFT baseline differs from the proposed architecture not in RF transfer efficiency, but in analog expressivity: it is limited to beam selection within a fixed Fourier basis.

VI. NUMERICAL RESULTS

We evaluate the proposed hybrid beamforming architecture in a *narrowband* multiuser downlink and compare it against (i) a fully-digital benchmark, (ii) FC1, the physically modeled Sohrabi–Yu fully-connected hybrid beamforming architecture proposed in [3] and explained in Subsection V-A, (iii) FC2, the physically modeled Yu–Zhang–Letaief fully-connected hybrid beamforming architecture proposed in [4] and explained in Subsection V-B, and (iv) the

ideal-lossless Garcia–Rodriguez *et al.* hybrid beamforming architecture with Butler/DFT beam-selection proposed in [2] and explained in Subsection V-C.

For the proposed architecture, we report results for both continuous phase-shifters and quantized phase-shifters with $q \in \{2, 4, 6\}$ bits. The fully-connected phase-shifter baselines are shown only with continuous phase-shifters, while the Butler/DFT baseline uses adaptive beam selection within a fixed DFT basis.

A. System setup

We consider a uniform linear array (ULA) with $N = 512$ antennas at $f_c = 100$ GHz and half-wavelength spacing $d = \lambda_c/2$. The proposed architecture uses $r = S = 16$ RF-chains/streams to serve $S = 16$ single-antenna users. The FC2 baseline also uses $r = S = 16$ RF-chains, while the FC1 baseline is evaluated in its exact-representation regime with $r_{\text{FC1}} = 2S = 32$ RF-chains, as prescribed by [3]. The Butler/DFT baseline is evaluated with $r_{\text{BM}} = r = S = 16$ selected DFT beams, i.e., the same number of RF-chains/beams as the proposed architecture. Guided by Proposition 2, we evaluate the depth sweep

$$M \in \{16, 32, 48, 64\} = \{S, 2S, 3S, 4S\}, \quad (82)$$

and use $M = 32$ for the injected-power sweep of Fig. 3. The fixed mixing layer \mathbf{W} is the unitary DFT (Butler) transform and is held fixed during optimization. All results are averaged over $N_{\text{MC}} = 500$ independent user locations and corresponding channel realizations.

We model the receiver-noise power from the thermal-noise density -174 dBm/Hz over a narrowband bandwidth $B = 200$ kHz, with no additional receiver noise figure. Thus,

$$\sigma_{\text{dBm}}^2 = -174 + 10 \log_{10}(B/\text{Hz}) = -120.99 \text{ dBm}, \quad (83)$$

which corresponds to

$$\sigma^2 = 10^{(\sigma_{\text{dBm}}^2 - 30)/10} = 7.96 \times 10^{-16} \text{ W}. \quad (84)$$

We evaluate Fig. 2 at

$$P_T = 0 \text{ dBm}, \quad (85)$$

and for Fig. 3 we sweep

$$P_T \in \{-20, -15, \dots, 50\} \text{ dBm}. \quad (86)$$

User k has distance $\rho_k \sim \mathcal{U}[50, 1000]$ m and angle $\theta_k \sim \mathcal{U}[-\pi/3, \pi/3]$, where the angle θ_k is measured with respect to the array axis. For the present array size and carrier frequency, the

Fraunhofer distance is approximately 400 m; hence the interval [50, 1000] m spans both Fresnel and Fraunhofer operating regions. We therefore refer to the model generically as a spherical-wave channel rather than a purely near-field channel.

a) *Spherical-wave geometric channel:* Let antenna n be located at

$$x_n = \left(n - 1 - \frac{N - 1}{2} \right) d. \quad (87)$$

For a path specified by (ρ, θ) , the spherical-wave distance from antenna n is

$$R_n(\rho, \theta) = \sqrt{\rho^2 + x_n^2 - 2\rho x_n \cos \theta}. \quad (88)$$

The channel to user k consists of one LOS path plus $L = 4$ NLOS paths:

$$\begin{aligned} [\mathbf{h}_k]_n &= \frac{\lambda_c}{4\pi\rho_k} e^{-j\frac{2\pi}{\lambda_c} R_n(\rho_k, \theta_k)} \\ &+ \sum_{p=1}^L \frac{\lambda_c}{4\pi\rho_{k,p}} \alpha_{k,p} e^{-j\frac{2\pi}{\lambda_c} R_n(\rho_{k,p}, \theta_{k,p})}, \end{aligned} \quad (89)$$

where $(\rho_{k,p}, \theta_{k,p})$ are i.i.d. draws from the same ranges as (ρ_k, θ_k) and $\alpha_{k,p} = 10^{-15/20} e^{j\varphi_{k,p}}$ with $\varphi_{k,p} \sim \mathcal{U}[0, 2\pi)$. The angle θ is measured with respect to the array axis, which is why the spherical-wave distance uses $\cos \theta$. Note that ρ_k and $\rho_{k,p}$ affect the channel through both spherical-wave phase curvature and the distance-dependent link budget.

Finally, we form the channel $\mathbf{H} = [\mathbf{h}_1, \dots, \mathbf{h}_S] \in \mathbb{C}^{N \times S}$, where the elements of \mathbf{h}_k are given by (89).

b) *Target for analog programming:* Following the subspace-synthesis viewpoint, we set the programming target \mathbf{F}_{tar} to an orthonormal basis of the dominant S -dimensional channel subspace. If

$$\mathbf{H} = \mathbf{U}\mathbf{\Sigma}\mathbf{V}^H \quad (90)$$

is the SVD of the narrowband channel matrix, then

$$\mathbf{F}_{\text{tar}} = \mathbf{U}(:, 1:S). \quad (91)$$

We choose $\mathbf{F}_{\text{tar}} = \mathbf{U}(:, 1:S)$ rather than the fully-digital MMSE precoder itself because the role of the analog stage is to synthesize the dominant transmit subspace, while stream weighting and interference regularization are handled by the digital MMSE stage computed from the effective channel.

The proposed architecture programs $\mathbf{F}_{\text{RF}}(\Phi)$ by solving (22) with Algorithm 1. The fully-connected phase-shifter baselines use the physical models in Section V, with continuous phases

and equal injected power. For the Butler/DFT baseline, the same target \mathbf{F}_{tar} is used to select the r_{BM} DFT beams with the largest scores $c_n = \|\mathbf{F}_{\text{tar}}^H \mathbf{u}_n\|_2^2$, as described in Subsection V-C.

c) *Digital stage, injected power, and rate metric.*: For the proposed architecture, once \mathbf{F}_{RF} is programmed, we form the effective channel

$$\mathbf{H}_{\text{eff}} = \mathbf{H}^H \mathbf{F}_{\text{RF}} \quad (92)$$

and compute the digital MMSE precoder

$$\mathbf{F}_{\text{BB}} = \mathbf{H}_{\text{eff}}^H (\mathbf{H}_{\text{eff}} \mathbf{H}_{\text{eff}}^H + \alpha \mathbf{I}_S)^{-1}, \quad (93)$$

where

$$\alpha = \frac{S\sigma^2}{P_T}. \quad (94)$$

The digital matrix is then scaled so that

$$\|\mathbf{F}_{\text{BB}}\|_F^2 = P_T. \quad (95)$$

Because the proposed analog stage is semi-unitary, this also implies $P_{\text{rad}} = P_T$.

For the fully-connected phase-shifter baselines, FC1 and FC2, the digital stage is recomputed over their corresponding effective channels and then scaled to satisfy the same injected-power constraint

$$\|\mathbf{F}_{\text{BB}}^{\text{FC1}}\|_F^2 = P_T, \quad \|\mathbf{F}_{\text{BB}}^{\text{FC2}}\|_F^2 = P_T. \quad (96)$$

Their radiated powers are

$$P_{\text{rad}}^{\text{FC1}} = \|\mathbf{F}_{\text{RF}}^{\text{FC1}} \mathbf{F}_{\text{BB}}^{\text{FC1}}\|_F^2 = \eta_{\text{FC1}} P_T \quad (97)$$

and

$$P_{\text{rad}}^{\text{FC2}} = \|\mathbf{F}_{\text{RF}}^{\text{FC2}} \mathbf{F}_{\text{BB}}^{\text{FC2}}\|_F^2 = \eta_{\text{FC2}} P_T \quad (98)$$

with $\eta_{\text{FC1}}, \eta_{\text{FC2}} < 1$ in general.

For the Butler/DFT baseline, the digital stage is recomputed over

$$\mathbf{H}_{\text{eff}}^{\text{BM}} = \mathbf{H}^H \mathbf{F}_{\text{RF}}^{\text{BM}} \quad (99)$$

and scaled to satisfy

$$\|\mathbf{F}_{\text{BB}}^{\text{BM}}\|_F^2 = P_T. \quad (100)$$

Because $\mathbf{F}_{\text{RF}}^{\text{BM}}$ is semi-unitary in the ideal-lossless model, the Butler baseline also satisfies

$$P_{\text{rad}}^{\text{BM}} = P_T. \quad (101)$$

The fully-digital benchmark is the unconstrained narrowband MMSE precoder computed directly from \mathbf{H} and scaled to satisfy

$$\|\mathbf{F}_{\text{FD}}\|_F^2 = P_T. \quad (102)$$

Hence all curves are compared at the same injected power P_T .

Treating residual multiuser interference as noise, the SINR of user s is

$$\text{SINR}_s = \frac{|\mathbf{h}_s^H \mathbf{f}_s|^2}{\sum_{j \neq s} |\mathbf{h}_s^H \mathbf{f}_j|^2 + \sigma^2}, \quad (103)$$

and we report the narrowband sum-rate

$$R_\Sigma = \sum_{s=1}^S \log_2(1 + \text{SINR}_s). \quad (104)$$

d) Optimization details.: For the proposed interlaced network, continuous-phase programming uses Adam with $(\beta_1, \beta_2, \epsilon) = (0.9, 0.999, 10^{-8})$, learning rate 0.02, and 500 iterations. For each channel realization and each depth M , we generate a pool of $N_{\text{rst}} = 2$ independent continuous-phase candidates. The continuous-phase curve uses the candidate with the largest subspace score $\|\mathbf{F}_{\text{tar}}^H \mathbf{F}_{\text{RF}}\|_F^2$.

For q -bit control with $q \in \{2, 4, 6\}$, every candidate in the same restart pool is first quantized elementwise to \mathcal{Q}_q and then refined by a greedy local discrete search with $N_{\text{sw}} = 12$ sweeps and candidate set $\{\phi, \phi \pm \Delta\}$, where $\Delta = 2\pi/2^q$, while enforcing the per-layer gauge $\phi_{1,k} = 0$. For each value of q , the final analog matrix is the refined q -bit candidate with the largest subspace score among the same restart pool; thus, each q -bit curve keeps its own best restart and is selected independently of the best continuous-phase design. The digital MMSE stage is then recomputed over the corresponding effective channel and scaled so that $\|\mathbf{F}_{\text{BB}}\|_F^2 = P_T$.

For Fig. 2, each depth M is optimized independently. The FC1 and FC2 baselines are shown with continuous phases only, while the Butler/DFT baseline uses adaptive beam selection only; once their analog matrices are fixed, their digital MMSE stages are recomputed over the corresponding effective channels and scaled to the same injected power.

B. Impact of depth: Figure 2

Guided by the stream-aware rule $M \approx 2S$, we evaluate the narrowband sum-rate at injected power $P_T = 0$ dBm for

$$M \in \{16, 32, 48, 64\}. \quad (105)$$

Figure 2 compares the fully-digital MMSE benchmark, the proposed architecture with continuous phases, the proposed architecture with 2-, 4-, and 6-bit phase quantization, the continuous-phase FC1 and FC2 baselines, and the Butler/DFT baseline.

Figure 2 shows that the proposed architecture benefits primarily from increasing the circuit depth up to about $M \approx 2S$, after which the returns diminish markedly. The continuous-phase and 6-bit realizations approach the fully-digital benchmark and then saturate, which is consistent with the stream-aware guideline of Proposition 2. The 4-bit realization follows the same qualitative behavior but with a persistent modest gap, whereas the 2-bit realization continues to improve with depth yet remains visibly below the higher-resolution cases.

The fully-digital benchmark and all three comparator baselines are horizontal because they do not depend on M . Among these depth-independent references, the ideal-lossless Butler/DFT beam-selection baseline is the strongest, but it remains clearly below the continuous-phase, 6-bit, and 4-bit realizations of the proposed architecture. The FC1 and FC2 baselines are substantially weaker under equal injected power, which is consistent with their contractive passive RF transport. Overall, Fig. 2 indicates that, for the present operating point, a depth around $M \approx 2S$ captures most of the attainable gain, while additional layers mainly provide marginal refinement. The gaps among the proposed continuous and quantized curves are due to analog-subspace mismatch rather than RF-transfer loss, because all proposed variants remain semi-unitary after phase quantization.

C. Sum-rate versus injected power

Motivated by the saturation around $M = 32$ in Fig. 2, we fix $M = 32$ and sweep the injected power P_T from -20 dBm to 50 dBm in 5 dB steps. Figure 3 compares the fully-digital MMSE benchmark, the proposed architecture with continuous phases, the proposed architecture with 2-, 4-, and 6-bit phase quantization, the continuous-phase FC1 and FC2 baselines, and the Butler/DFT baseline.

Figure 3 shows that the proposed architecture with continuous phases remains essentially indistinguishable from the fully-digital benchmark across the entire injected-power range. The 6-bit realization follows it almost exactly, while the 4-bit realization stays close with only a small persistent loss. The 2-bit realization exhibits a more visible gap, but it still improves monotonically with injected power and preserves the same qualitative scaling trend.

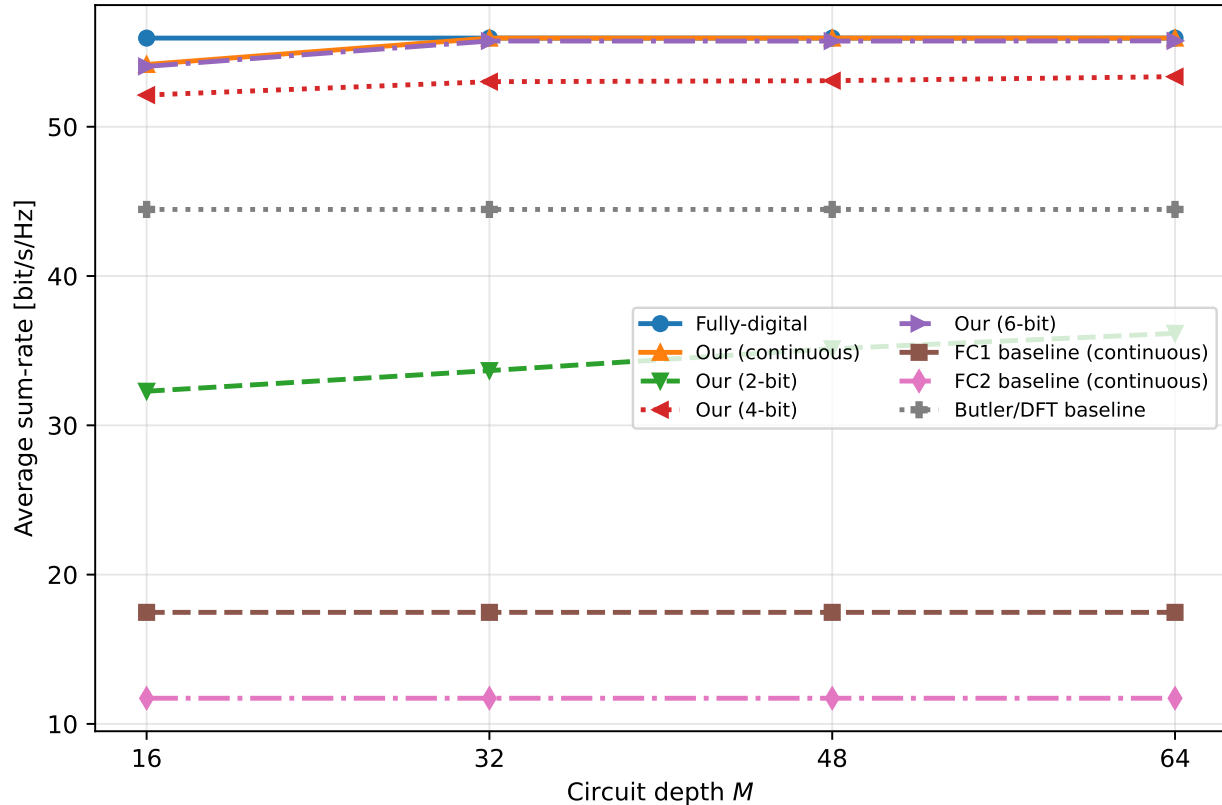


Fig. 2. Narrowband average sum-rate versus depth M at injected power $P_T = 0$ dBm for $N = 512$ and $S = r = 16$. The proposed architecture is shown for continuous phases and for 2-, 4-, and 6-bit phase quantization followed by greedy local discrete refinement; the FC1 and FC2 baselines are shown with continuous phases only, and the Butler/DFT baseline uses adaptive beam selection within a fixed Fourier basis. The proposed continuous-phase and 6-bit curves saturate near $M \approx 2S = 32$.

Figure 3 also shows that the proposed hybrid beamforming architecture achieves significant performance gains over the FC1, FC2, and Butler/DFT baselines. Compared with FC1 and FC2, the gains of the proposed architecture arise primarily from the fact that its RF transport remains semi-unitary under equal injected power, whereas the passive fully-connected baselines are physically contractive. Compared with the Butler/DFT baseline, the gain arises from greater analog-subspace programmability rather than from any proved universal approximation property. Accordingly, the main message of Fig. 3 is empirical: in the present setup, the proposed continuous-phase and 6-bit realizations nearly reproduce the fully-digital benchmark, while the remaining gap of the lower-resolution designs is governed by analog-subspace mismatch.

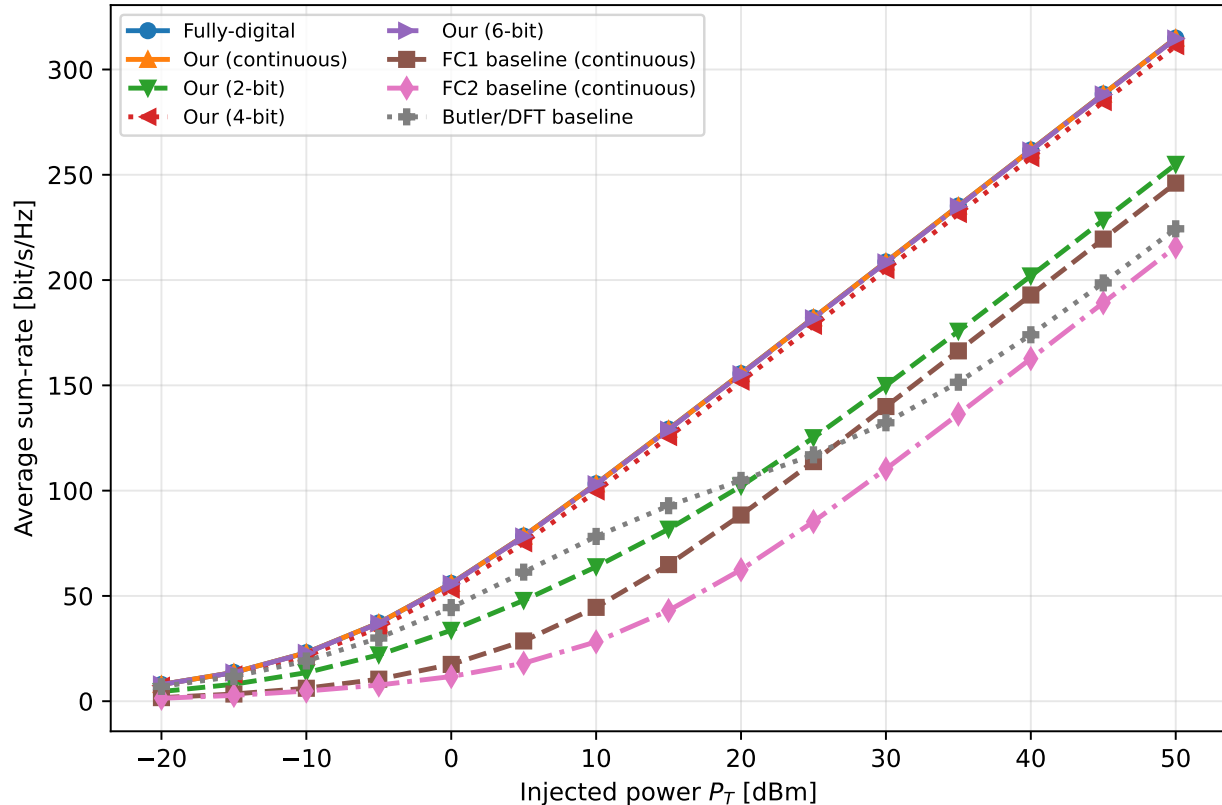


Fig. 3. Narrowband average sum-rate versus injected power P_T (in dBm) for $M = 32$, $N = 512$, and $S = r = 16$. The proposed architecture is shown for continuous phases and for 2-, 4-, and 6-bit phase quantization followed by greedy local discrete refinement; the FC1 and FC2 baselines are shown with continuous phases only, and the Butler/DFT baseline uses adaptive beam selection within a fixed Fourier basis. In this $S = 16$ setting, the continuous-phase and 6-bit realizations of the proposed architecture are nearly indistinguishable from the fully-digital benchmark across the entire injected-power range.

VII. CONCLUSION

This paper proposed a hybrid beamforming architecture based on a programmable unitary RF network and studied its performance from an equal-injected-power viewpoint in the narrowband setting. Because the induced analog beamformer is semi-unitary, the architecture preserves the injected RF-chain power exactly at the antenna ports under the ideal matched hardware model. Importantly, this power-preserving property survives phase quantization: quantizing the programmable phase layers reduces the reachable analog subspace, but it does not change the semi-unitarity of the analog processor and therefore does not alter the equal-injected-power normalization. This property sharply distinguishes the architecture from passive fully-connected hybrid beamforming architectures whose RF transfer is contractive.

We derive a closed-form digital beamformer and a low-complexity programming method for the analog beamformer, which together produce a hybrid precoder that closely matches the fully-digital precoder. We also derive a stream-aware depth guideline for the interlaced mixer–phase architecture.

The numerical results for the spherical-wave downlink show that the proposed hybrid beamforming architecture can closely reproduce the performance of the fully-digital architecture while providing significant performance gains over the baseline architectures under equal injected power.

REFERENCES

- [1] R. W. Heath, Jr., N. Gonzalez-Prelcic, S. Rangan, W. Roh, and A. M. Sayeed, “An overview of signal processing techniques for millimeter wave MIMO systems,” *IEEE Journal of Selected Topics in Signal Processing*, vol. 10, no. 3, pp. 436–453, 2016.
- [2] A. Garcia-Rodriguez, V. Venkateswaran, P. Rulikowski, and C. Masouros, “Hybrid analog–digital precoding revisited under realistic RF modeling,” *IEEE Wireless Communications Letters*, vol. 5, no. 5, pp. 528–531, Oct. 2016.
- [3] F. Sohrabi and W. Yu, “Hybrid digital and analog beamforming design for large-scale antenna arrays,” *IEEE Journal of Selected Topics in Signal Processing*, vol. 10, no. 3, pp. 501–513, Apr. 2016.
- [4] X. Yu, J. Zhang, and K. B. Letaief, “Doubling phase shifters for efficient hybrid precoder design in millimeter-wave communication systems,” *Journal of Communications and Information Networks*, vol. 4, no. 2, pp. 51–67, Jun. 2019.
- [5] M. Reck, A. Zeilinger, H. J. Bernstein, and P. Bertani, “Experimental realization of any discrete unitary operator,” *Physical Review Letters*, vol. 73, no. 1, pp. 58–61, Jul. 1994.
- [6] W. R. Clements, P. C. Humphreys, B. J. Metcalf, W. S. Kolthammer, and I. A. Walmsley, “Optimal design for universal multiport interferometers,” *Optica*, vol. 3, no. 12, pp. 1460–1465, Dec. 2016.
- [7] R. Keshavarz, K. Zelaya, N. Shariati, and M.-A. Miri, “Programmable circuits for analog matrix computations,” *Nature Communications*, vol. 16, p. 8514, Sep. 2025.
- [8] J. Álvarez-Vizoso and D. Barral, “Universality and optimal architectures for layered programmable unitary decompositions,” *arXiv preprint arXiv:2510.19397*, Oct. 2025.
- [9] X. Gao, L. Dai, S. Han, C.-L. I, and R. W. Heath, Jr., “Energy-efficient hybrid analog and digital precoding for mmWave MIMO systems with large antenna arrays,” *IEEE Journal on Selected Areas in Communications*, vol. 34, no. 4, pp. 998–1009, Apr. 2016.
- [10] Z. Wu, M. Nerini, and B. Clerckx, “Microwave linear analog computer (MiLAC)-aided multiuser MISO: Fundamental limits and beamforming design,” *arXiv preprint arXiv:2601.10060*, Jan. 2026.